Ageing Analysis and Asymmetric Stress Considerations for Small Format Cylindrical Cells for Wearable Electronic Devices

C. C. Tan [a], M. Walker [b], G. Remy [a], N. Kourra [a], F. Maddar [a], S Dixon [a], M. Williams [a], M. J. Loveridge [a]

a) Warwick Manufacturing Group (WMG), University of Warwick, Coventry, CV4 7AL, UK
b) Department of Physics, University of Warwick, Coventry, CV4 7AL, UK

Corresponding Author:

Chaou C Tan

Address: WMG, University of Warwick, Coventry, CV4 7AL, UK
Tel: +44 (0) 781 888 3384
Email: chaou.c.tan@gmail.com, c.tan.18@warwick.ac.uk

Type of paper:	Research paper
Word count:	5761
Number of Tables:	1
Number of Figures:	8
Number of References:	55

Abstract

Performance assessments on miniature cylindrical cells used in Fitbit Flex 2 fitness trackers have been performed to understand the dominant ageing modes and small format implications. We utilise electrochemical testing, x-ray photoelectron Spectroscopy (XPS), x-ray computed tomography (XCT) and scanning electron microscopy (SEM), to reveal device and component structural features and changes. The cell maintains 82% cell capacity retention after 500 continuous charging and discharging cycles at 3.0-4.35V, 0.75C rate at 20 °C. The anode shows severe delamination due to high bending stress exerted on the cell components, however this seemingly has minimum impact on the electrochemical performance if the coating is sufficiently compressed in the jelly roll with a good electrical contact. After ageing, the surface layers continue to grow, with more LiF found on the cathode and anode. The formation of LiF is discussed and we suggest the main ageing mechanism of the Fitbit cell is related to increasing charge transfer resistance due to the transportation of Li^+ ions being inhibited by the thicker surface layer, which contains LiF. That preferential delamination on the inner sides of the electrode coatings was observed consistently opens up an interesting avenues for advances in cylindrical cell manufacturing at large.

Keywords

1. Introduction

Batteries for medical applications and wearable devices continue to evolve in size and shape, with miniaturisation of Li-ion technologies becoming increasingly popular in recent years [1]. However, as the size of the battery shrinks, the fabrication process for composite electrodes and the use of liquid electrolyte becomes a processing challenge for microfabrication using conventional approaches [2]. $LiCoO_2$ (LCO) is still commonly used for portable and wearable devices despite continued concerns about cobalt being toxic and expensive [3]. The development of all-solid state microbatteries has been widely investigated and LCO has remained the most common choice of cathode for these small formats [4]. Lithium nickel manganese cobalt layered oxide (NMC) has gradually found applications in portable devices such as laptops and e-cigarettes, however it is believed that LCO will still dominate smaller, wearable devices due to its higher voltage platform and volumetric energy density [5].

Following the initial reported performance benefits of LCO, it was later discovered that LCO cells have large impedance issues due to the growth of high surface layer resistance and charge transfer resistance, which causes a drop in capacity, with the cathode resistance dominating the overall resistance of the cell upon cycling [4]. The increasing impedance was deemed attributable to the growth of a surface layer on the both the anode (solid electrolyte interface, SEI) and cathode (cathode electrolyte interface, CEI) due to the reaction between the electrodes and the electrolyte [6].

An increase in the cell impedance in LCO after cycling or calendar aging has been commonly observed in the literature [6-12] and has confirmed that the growth of SEI and CEI (cathode/electrolyte interface) can have a significant impact on the capacity fading [7, 10, 13-18]. This degradation occurs only on the surface rather than the bulk. X-ray photoelectron spectroscopy (XPS) studies show that surface compositions are mainly composed of an inner layer of inorganic materials (LiF, Li_2O, Li_2CO_3) and a porous outer layer composed mainly of organic materials (oligomer species and semi-carbonates) [13-16, 19-21].

The surface SEI and CEI layers have varying thicknesses between 15 to 25 Å [22] and the SEI/CEI adds an additional boundary for the Li^+ ion to diffuse between the electrode and electrolyte during charging

and discharging, thus slowing down the transfer process especially when SEI/CEI has lower ionic conductivity. It has been shown by several studies that the SEI/CEI is the rate limiting step for the charge transfer process in non-aqueous lithium ion batteries [8, 11, 22, 23].

It is well accepted that the dominating degradation mechanism for anode is related to the growth of SEI on the anode and tend to be thicker than corresponding surface layers on the cathode due to the aprotic electrolyte being thermodynamically unstable against electrochemical reduction [24]. LiF is one of the main SEI/CEI components in $LiPF_6$ based electrolyte system [7, 17, 25] and it is generally accepted that LiF inhibits Li^+ migration at the electrode-electrolyte interface and thus leads to capacity fade of the LCO cell. DFT calculations by Pan and Cheng [26] shows that the LiF ionic conductivity on the cathode (10^{-31} Scm^{-1}) is lower than that on the anode (10^{-12} Scm^{-1}), and this implies that the thinner LiF on the cathode can induce a larger charge transfer resistance than the thick LiF on the anode. In addition, the LCO active material itself can be subjected to degradation when in contact with electrolyte [18, 27, 28]. Takamatsu et al. [18] showed that the Co ion on the surface of $LiCoO_2$ can be reduced from Co^{3+} to Co^{2+}, forming an irreversible compound such as Co_3O_4 when immersed in the organic electrolyte, and this process is accelerated in the presence of water [27, 28]. It has also been shown that LCO subjected to extensive cycling ageing can lead to localised irreversible phase transition initiating on the LCO surface, from trigonal O3 phase to H1-3 phase and then to cubic spinel ($Li_{1+y}Co_2O_4$). These oxide layers can lead to high charge transfer resistance [18, 29, 30]. Current commercial LCO cells now have an upper voltage limit of 4.35 - 4.4 V [12] yielding an additional 10% of energy density increase [29, 31] compared to when charging to 4.2 V. Many studies have reported improvement in capacity retention when the upper voltage limit is increased [9, 13-15, 31-37] but only a few studies were conducted in a full cell [12, 38]. Nelson et al [12] reported an ageing test on commercial LCO cells cycled at 4.2 and 4.4 V, respectively, followed by 24 h dwell at the upper voltage limit before discharge to replicate the "real-life" or the practical mobile phone battery ageing scenario. They reported a larger R_{ct} when the cells are charged to 4.4 V when compared to 4.2 V. The differential voltage analysis showed that the cell capacity loss when charged to 4.2 V is dominated by SEI growth

on the anode, whereas severe damage on the cathode dominates the capacity loss when charge to 4.4 V. Unfortunately, no post-mortem analysis was performed, which could have provided valuable information to validate the SEI status through appropriate materials characterisation. When charged above 4.2 V, the LCO cell suffered capacity loss which has been shown to be related to the structural instability due to phase transition from hexagonal (O3 phase) to monoclinic phase [29, 32]. Even higher capacity loss has been reported when transitioning from O3 phase to H1-3 and O1 phase at 4.55 V [29, 34]. Operating at high voltage can lead to fatal structure damage which results in oxygen loss, Co dissolution into the electrolyte, elastic strain and stacking faults within the LCO particles [29, 32, 34, 37].
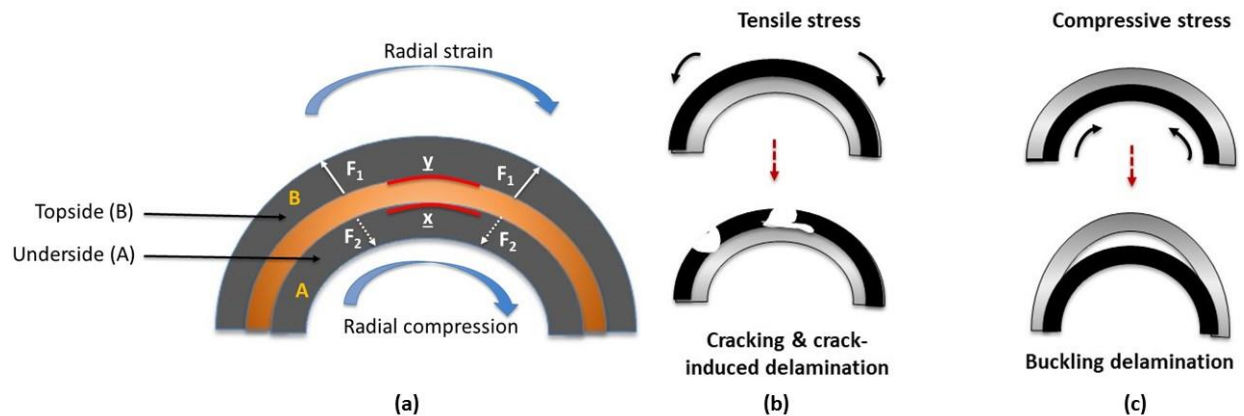

Fig. 1 (a) *A schematic illustration of a section of an anode in a cylindrical cell (bending radius is arbitrary as this would vary in gradient from the outside to the inside of a jelly roll); where red line x = interface between the current collector and inner-facing coating side A and red line y = interface between current collector and outer-facing anode coating side B. F1 and F2 are the uniaxial forces of strain and stress for the respective outer and inner-facing coating sides. Modes of coating interface damage due to **(b)** tensile stress and **(c)** compressive stress.*

This study also highlights potential sources of physical deterioration in the battery components emanating from the manufacturing process. Processing artefacts can be a contributing source of increased internal resistance and diminishing capacity. We postulate that there are inherent stresses exerted on the electrode-current collector interfaces resulting from the winding configuration in cylindrical cells, and this stress will be asymmetrical in nature. Fig. 1 (a) schematically illustrates the situation experienced by a wound double-sided coating section (as exists within a cylindrical cell).

Coating side A will be subjected to a greater degree of compressive stress than side B, which will experience more radial strain or tension, as a function of the winding direction. This will then create a differential in bended surface area between the 2 sides of the same coating. The implications of this will affect the respective interfacial bond quality and mechanical responses (especially during operation, when active particles can expand and generate additional internal coating stress.) As such, both adhesive and cohesive shearing can be a simultaneous degradation phenomena and compromise electrode interfacial integrity [39, 40].

Compressive stresses on coatings can cause buckling delamination (affecting adhesion) and tensile stress will potentially affect more on the cohesion through cracking but also adhesion through disbondment [41, 42] by circumferential tension. This is schematically illustrated in Fig. 1 (b) and (c). From an electrochemical perspective, we report our ageing and characterisation study on a commercial cell extracted from a fitness device, the Fitbit Flex 2. Disassembly of the fitness tracker, revealed a 15 mAh miniature cylindrical cell (a pin cell) with dimensions of 3.65 x 20 mm and an energy density of 503 Wh/L. To the best of our knowledge, no studies have yet been reported on this particular cell type. In this study, we perform electrochemical impedance spectroscopy (EIS), followed by cell disassembly to extract electrode sections for x-ray photoelectron spectroscopy (XPS) and scanning electron microscopy (SEM) characterisation in order to elucidate the ageing process of Fitbit Flex 2 cell.

2. Experimental Section

2.1 X-ray Computed Tomography (CT) Scan

X-ray Computed Tomography (XCT) was performed using a Zeiss Versa 520 XCT scanner on both the Fitbit device and on the cell. XCT reconstructs a series of radiographs to a 3D model that includes the inner and outer geometry of the specimen. The scanning settings are shown in Table 1. These setting were chosen to achieve optimum results based on the greyscale values (brightness of a pixel) achieved

on the radiographs to provide sufficient penetration whilst minimising noise. Objects with lower atomic number (lower attenuation to the x-ray beam) exhibits darker grey values and vice versa.

Table 1. *X-ray computed tomography (XCT) scanning settings used for analysing Fitbit cell device and Fitbit cell.*

CT Scanning settings	
Voltage (kV)	140
Power (W)	10
Exposure Time (sec)	11
Voxel Size (µm)	16.75
Filtration	HE4

2.2 Electrochemical Test

Electrochemical characterisation was performed using a Biologic VMP3 potentiostat, with a BH-1i battery holder in a BINDER climate chamber set to 20 °C. For the variable rate testing, the cells were charged and discharged between 3.00 - 4.35 V at a constant current (CC) of C/10 followed by C/5, C/3, C/2, ¾ C, 1C and C/10 with 10 cycles at each C-rate. A constant voltage (CV) step at 4.35 V was performed after the charging step, with the current tapered to one-tenth of the current used in the CC step. In this study, 1 C is 15 mA which is based on the cell capacity (15 mAh) provided by the cell manufacturer. Alternating current impedance was performed across a frequency range of 50 kHz- 100 mHz at 3.5 V and 4.3 V for every cycle.

For the lifespan cycle testing, cells were charged and discharged between 3.00 - 4.35 V at ¾ C with a CV step at 4.35 V until the current tapered to C/20. This process was repeated for 100, 200 and 500 cycles for the respective cells. AC impedance was performed using the same frequency range and voltage limits as outlined above for every 10 cycles.

2.3 Cell Post-mortem Analysis

Cells were discharged at 20° C to 3.0 V prior to any disassembly for analysis, which were performed in an argon filled MBraun MB200-G glovebox, with the H_2O and O_2 levels in the glove box maintained at < 5 ppm. The cylindrical metal casing was carefully removed and the jelly roll was unravelled for visual inspection using scanning electron microscopy (SEM) and x-ray photoelectron spectroscopy analysis (XPS) for the chemical identification of surface species.

2.4 X-ray Photoelectron Spectroscopy (XPS)

Surface chemical compositions were measured using x-ray photoelectron spectroscopy (XPS). A Kratos Axis Ultra DLD spectrometer (Kratos Analytical Ltd) was used, with monochromatic Al-Kα (hv = 1486.7 eV) used to illuminate the sample surface. High resolution spectra were obtained using 20 eV pass energy (approximately 0.4 eV resolution) with analysis area of ~300 - 700 μm. XPS samples were prepared in the glovebox and transferred to the XPS chamber via an inert transfer unit to avoid any surface changes when exposed to humid air. A charge neutraliser was used during the experiments in order to prevent surface charging. Peak fitting was performed using the CasaXPS software, using mixed Gaussian-Lorenztian (Voigt) lineshapes and Shirley backgrounds, with all spectra energy-referenced to the C-C component of the C 1s region at 284.8 eV.

2.5 Scanning Electron Microscopy (SEM)

The surface microstructure of the cathode, anode and separator were examined using a Carl Zeiss Sigma field-emission scanning electron microscope (FE-SEM). The separator had gold and palladium sputtered onto the surface using a sputter coater, in order to mitigate surface charging during SEM analysis. Elemental analysis was carried out using energy-dispersive spectroscopy (EDS) with AZtec software (Oxford Instruments).

3. Results and Discussions
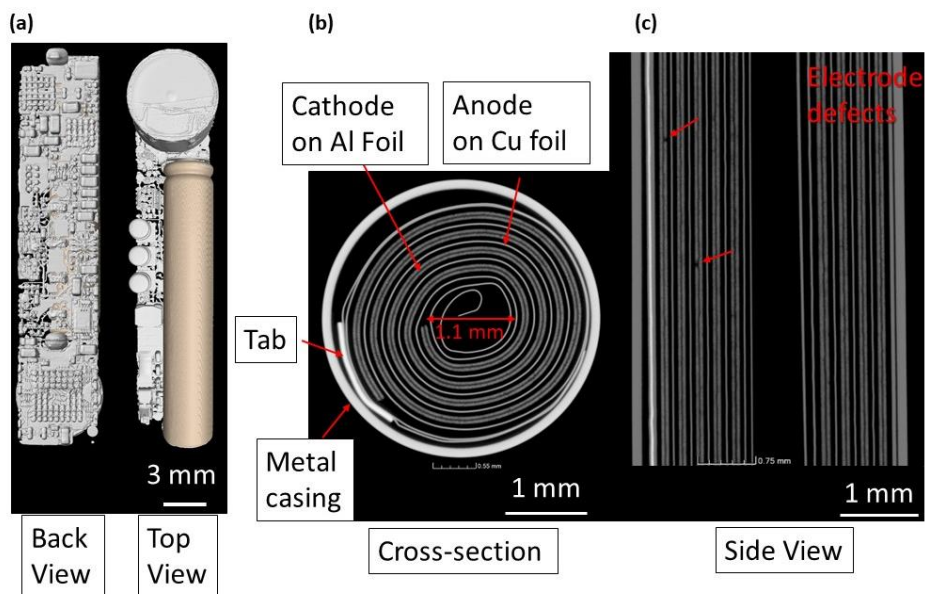
3.1 X-ray Computed Tomography (XCT)

Fig.2. X-ray computed tomography (XCT) scan of (a) the as-received Fitbit device showing the top and back view, and the cylindrical cell from Fitbit showing (b) cross-section and (c) side view of the Fitbit cell.

XCT was used to locate the cell in the Fitbit Flex 2 before opening. Fig. 2 (a) shows the top and bottom view of the tracking device, revealing a miniature cylindrical cell and the corresponding electronic components. The cell has dimensions of 3.65 mm diameter and 20 mm length. After removing the cylindrical cell from the fitness tracker, further XCT inspection reveals a jelly roll with an outer diameter of ~ 3.3 mm and inner diameter of ~1.1 mm, Fig. 2 (b). Note the outer diameter of the jelly roll is similar to the diameter of a mandrel core in an 18650 cylindrical cell. The side view of the jelly roll reveals some minor defects on the electrode, Fig. 2 (c). Overall, the XCT scan does not show any obvious defects or severe deformation of the electrode that could to lead to the sudden failure of the cell.

3.2 Electrochemical Data

Fig. 3 (a) shows the cell capacity versus cycle number with variable C-rate for the Fitbit cell. The C-rate varies from C/10, C/5, C/3, C/2, ¾ C and then 1C.
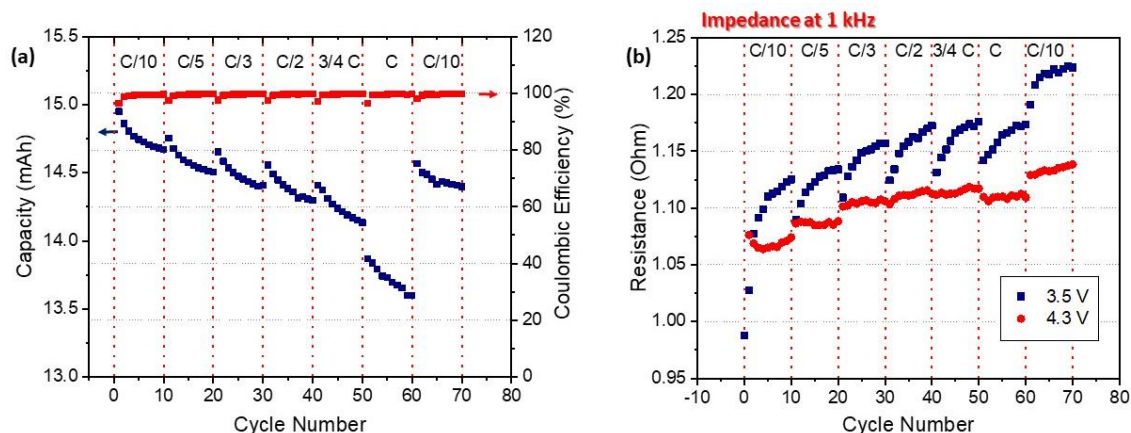

Fig. 3. (a) Capacity and *(b)* Impedance at 1 kHz vs cycle number plot for the Fitbit cell cycling at variable C-rate.

The cell capacity is C-rate dependant and as the rate increases, the cell capacity decreases accordingly. The cell is once more cycled at C/10 following the rate-variable cycling and the cell capacity has reduced by 3 %. Impedance measurements were taken during each cycle at 3.5 and 4.3V respectively, and demonstrate that the cell impedance at 1 kHz increases with increasing C-rate, Fig. 3 (b).

Fig. 4 (a) shows the charge and discharge voltage plots of a Fitbit cell following 500 cycles. The voltage plot does not show apparent plateaus but does indicate a gradual drop in cell capacity from 14.3 to 11.7 mAh. The cell shows a linear drop in capacity and has a cell retention capacity of 81.8% with an average coulombic efficiency of 99.89 %, Fig. 4 (b). The differential capacity plot, Fig. 4 (c), shows two peaks which correspond to lithium intercalation on the graphite (3.8 V) and also a H_1 to H_2 $LiCoO_2$ phase transition (3.9 V) [43]. The peaks intensities however, decreased, broadened, and shifted to higher voltage indicating an increase in the internal resistance with increasing cycle number. This was corroborated by impedance measurement at 1 kHz measured at 4.3 V and 3.5 V as shown in Fig. 4 (d), and the corresponding increase in the resistance by 48.8% and 37.2 % at 3.5 V and 4.3V, respectively.
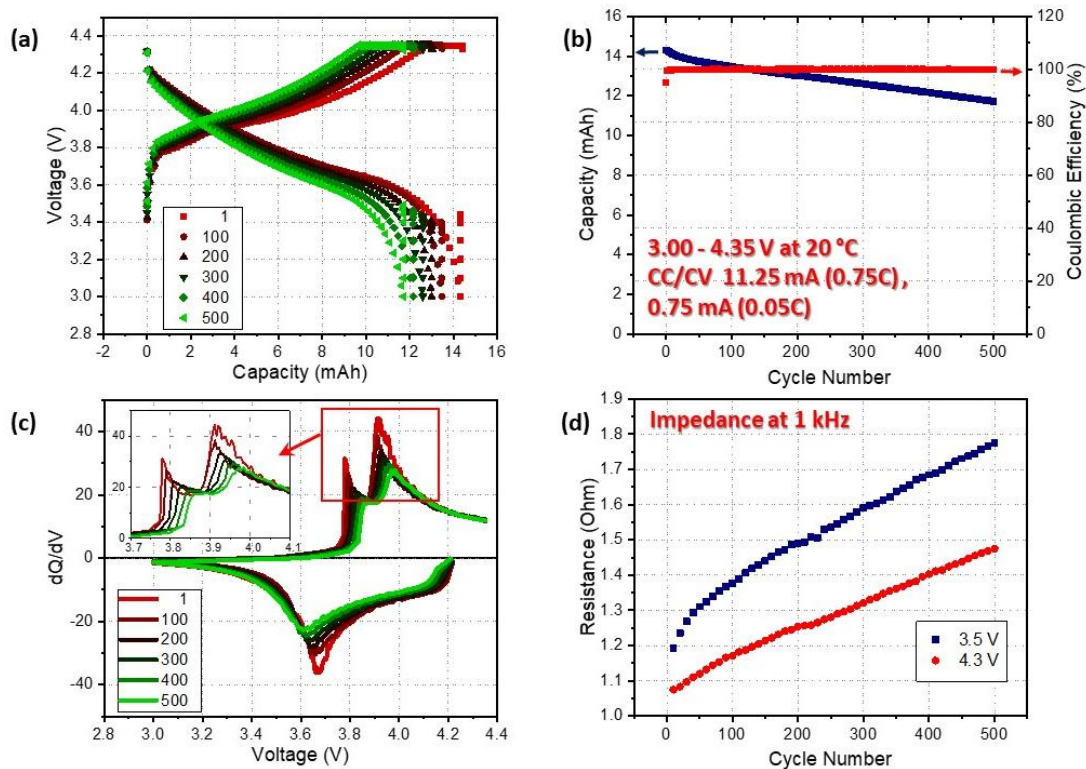
Fig. 4 (a) *Voltage plot,* **(b)** *cycle life,* **(c)** *differential capacity plot at different cycle number and* **(d)** *Impedance at 1 kHz at 3.5 V and 4.3 V for Fitbit cell.*

3.3 Post-mortem Analysis

The as-received Fitbit cell was disassembled and the condition of the cathode and anode are shown in Fig. 5 (a). The inward facing cathode (under tension) when rolled into a jelly roll, showed no sign of coating delamination from the aluminium foil. On the outward facing cathode side (under compression), however, a partial delamination was evident and the coating was transferred unto the separator. By contrast, severe delamination was observed on both sides of the anode coating. The inward facing anode side (under compression) showed almost no coating still adherent to the copper foil, compared to the outward facing anode side (under tension). Likewise, the delaminated coating had become adhered to the separator during operation.
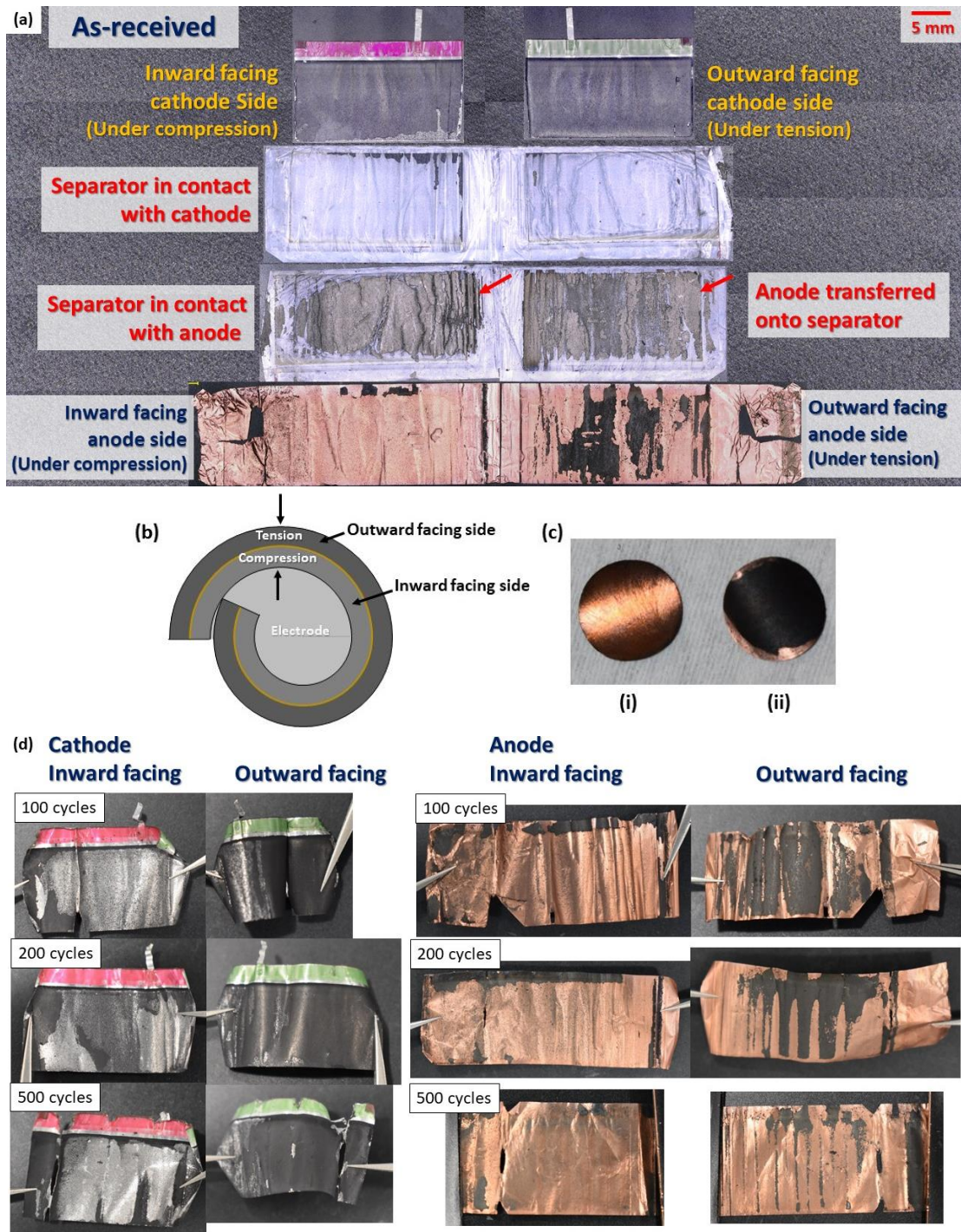
Fig. 5 (a) A disassembled as-received Fibit cell at OCV 3.2V showing the condition of the cathode, anode and the separator.

(b) A schematic illustration of a section of an anode in a cylindrical cell showing electrode under tension and compression. (c)

Sections taken from a commercial 21700 cylindrical cell anode coating of (i) Inner facing side and (ii) Outward-facing side. (d)

Disassembled Fitbit cell showing the condition of the cathode and anode after 100, 200 and 500 number of charge cycles.

It is interesting to note that, for both the cathode and the anode, the delamination is more severe on the electrode coating side that would have been subjected to compression stress, rather than tensile strain. This can be further explained by considering the asymmetric forces in place on either side of double side coated electrodes, Fig. 5 (b). Fig. 5 (c) shows disc of electrodes cut out from commercial 21700 cylindrical cells from the inner –facing and outer-facing abide coating sides (towards the centre of the jelly roll).

Fitbit cells that had undergone 100, 200 and 500 cycles were also disassembled and are shown in Fig. 5 (d). Consistent with the aforementioned findings, more severe delamination is observed on the compression side when compared to the tension sides for both cathode and anode. Most of the cathode and anode materials had transferred to the separator, Fig. S1 in supplementary material. For the cathode, more delamination was observed after cycling, however, the amount of delamination does not clearly correlate with the number of cycles. Similarly, more severe delamination is also observed on the compression side compared with tensioned sections for both cathode and anode. The severe anode delamination upon disassembly may be due to brittle nature of graphite when rolled to a 3.3 mm diameter jelly roll.

Whilst the Fitbit cell had severe anode coating delamination upon disassembly, the cell showed 82 % capacity retention after 500 cycles of charging and discharging. Severe delamination exaggerated by disassembly is due to weakening of adhesion between the anode materials and the copper current collector due to high bending stress and aging phenomena exerted on the cell components when rolled up to a 3 mm diameter jelly roll with 1 mm inner diameter.

It is challenging to ascertain the level of delamination prior to unrolling the layers, with the consequence of delamination minimal, salvaged by compression keeping components in electrical contact in the cylindrical cell format. However, further investigation is required to confirm this hypothesis.

A study conducted by Mohanty et al. [44] showed the defective $LiNi_{0.5}Mn_{0.3}Co_{0.2}O_2$ (NMC532) electrode with agglomeration, pinholes, metal particles contaminants and non-uniform coatings

results in poor rate capability, especially when cycled at higher C-rates. However, if the defects are small (pinholes of 0.1 - 0.2 mm, agglomerates of 0.05 - 0.1 mm and 1 mm width line defect), the effect on the overall electrochemical cell performance is minimal (cycled at 1 C). These defective electrodes maybe salvageable for grid storage application where a lower C-rate is required [45].

3.4 X-ray photoelectron Spectroscopy (XPS)

The as-received and aged (500 cycles) cathode and anode were examined in the discharged state. Survey spectra (0 – 1400 eV) were first collected to identify the elements present on the electrode surface before high resolution core level spectra were acquired (C 1s, O 1s, F 1s, N 1s, P 2p, S 2p, Li 1s, Co 2p and Na 1s). The atomic concentrations (at %) of various elements detected on the surface of each sample are summarised in supplementary materials, Table S1.

The CEI layer was observed on the as-received cathode with the XPS analysis showing an upper layer comprised mainly of carbon (48.9 at %), oxygen (16.6 at %) and fluorine (23.4 at %), attenuating the signal from the underlying cobalt (1.5 at %). A small amount of phosphorous (0.9 at %) and lithium (5.6 at %) was also detected. Small amounts of sodium, nitrogen and sulphur were also detected, most likely due to impurities or unknown electrolyte additives in the cell. Nitrile-based additives such as N-(triphenylphosphoranylidene) aniline (TPPA, 26), fumaronitrile (FN, 30), adiponitrile (ADN, 31) and sulfone based electrolyte additives such as trans-3-Methyl-2-hexenoic acid– bistriflimide (TMTA-TFSI) and dipropyl disulphide (DPDS) were tested in LCO systems and have shown to improve capacity retention when charged to higher voltage [5]. No further analysis was carried out on sodium, nitrogen and sulphur in this study to confirm the provenance of these elements.

The atomic concentration of carbon, fluorine and oxygen between as-received and the 500 cycled cathode are similar, however, the phosphorous and lithium content show a slight increase in the 500 cycled cathode. Cobalt is lower in the 500 cycle sample (0.72 at %) and indicates the growth of CEI layer obscuring detection the LiCoO$_2$ active material, owing to the limited sampling depth from which photoelectrons are detected without suffering energy losses.

Similarly, the surface layer SEI on the anode was observed on both the as-received and 500 cycle anodes. The SEI layers are dominated by carbon (56.9 at %), oxygen (21.9 at %) and fluorine (9.0 at %). 8.4 at % of lithium is also observed on as-received anode. For 500 cycled anode, carbon content is lower than as-received but fluorine (20.0 at %) and lithium (18.1 at %) are twice the amount. It is worth noting that no cobalt is detected on both as-received and 500 cycled anode surface indicating the absence of cobalt dissolution which is observed when the cell is cycled above 4.5 V [29].

The F $1s$ spectra for the as-received cathode shows a single broad peak which is composed mainly of electrolyte salt, $LiPF_6$, PVdF (CH_2-CF_2) binder and also $Li_xPF_yO_z$, Fig. 6 (a). $Li_xPF_yO_z$ is a degradation product of $LiPF_6$ through hydrolysis process [14, 15, 46] and 14.2 at % of $Li_xPF_yO_z$ is observed indicating moisture may have been introduced to the cell during cell assembling process. This may also explain the presence of 1.2 at % LiF (685.1 eV) which is also a decomposition of $LiPF_6$ through reaction with moisture. The formation of LiF will be further discussed in section 3.6.

After 500 cycles, LiF increased to 4.9 at %, however $Li_xPF_yO_z$ decreased to 9.2 at %. The slight reduction of $Li_xPF_yO_z$ may be due to further decomposition to form LiF. Peak assignment (Table S2) of the fluorine peaks and associated references can be found in supplementary material.

 On the anode, the F $1s$ spectra have broadly the same structure, with LiF, $LiPF_6$, $Li_xPF_yO_z$ and PVdF (CH_2-CF_2) observed. The presence of CH_2-CF_2 on anode shows that PVdF binder is used as opposed to water based binder systems such as NaPAA, poly (acrylic acid sodium) and CMC, carboxymethyl cellulose binder. In contrast to the cathode, only 3.4 at % of $Li_xPF_yO_z$ is observed and the amount is very similar (4.0 at %) in the 500 cycled anode. However, slightly higher LiF (2.0 at %) is observed on the as-received anode, essentially double the amount observed on the cathode. The contribution assigned to LiF again markedly increases, rising by a factor of 6 (to 11.4 at %) after 500 cycles.
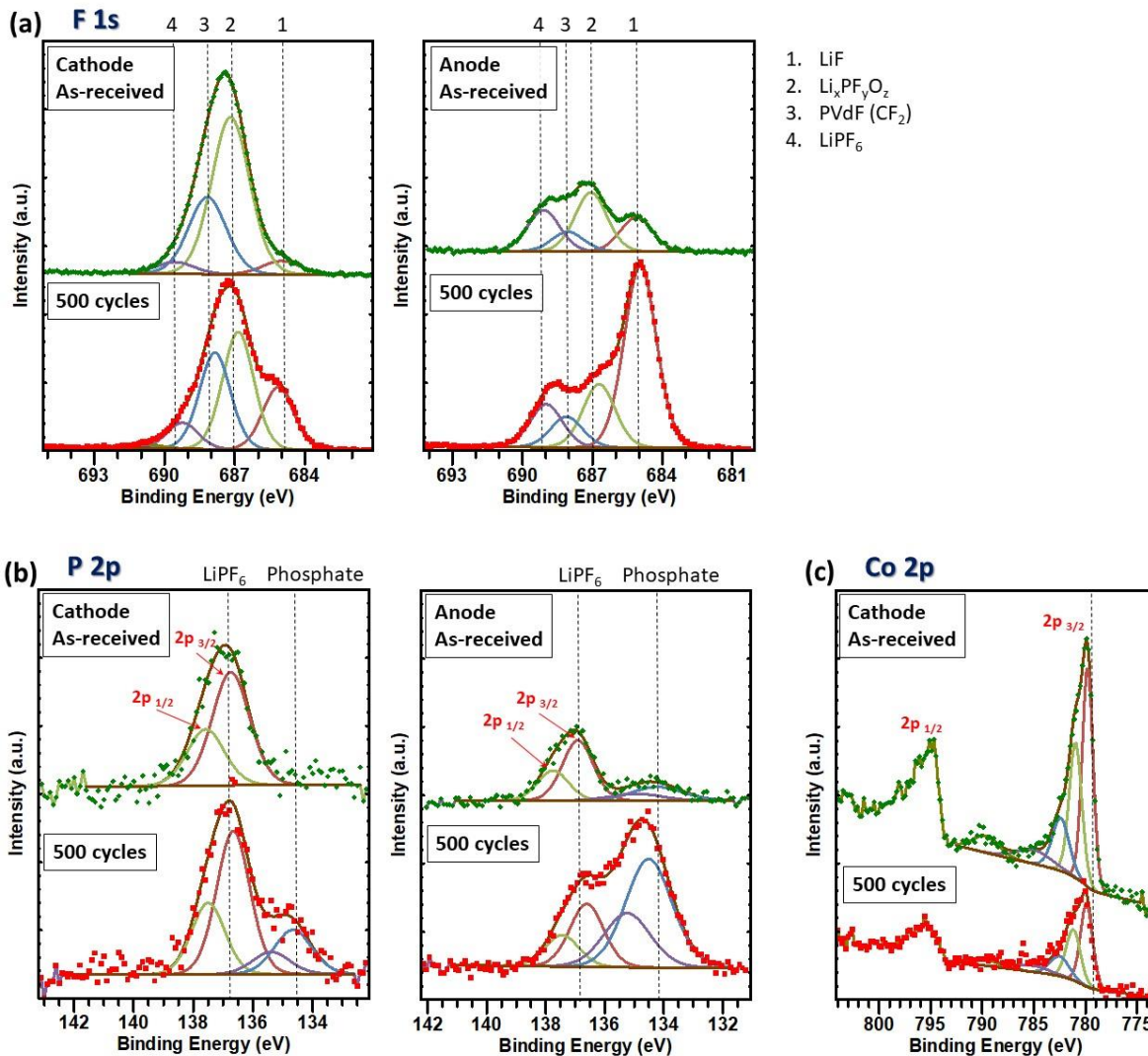
Fig. 6. *XPS spectra of as-received and cycled cathode and anode for (a) F 1s, (b) P 2p and (c) Co 2p.*

The P 2p spectra, Fig. 6 (b), for the as-received cathode showed one set of doublet peaks with binding energy of 136.7 eV ($2p_{3/2}$) and 137.6 eV ($2p_{1/2}$), respectively, corresponding to P-F bonding from LiPF$_6$. [14, 15, 46] On the 500 cycle cathode, an additional doublet was observed at a lower binding energy (134.7 eV and 135.4 eV) which may correspond to phosphate ending PEO oligomers R-(O-CH$_2$-CH$_2$)$_n$-OPO(OR)$_2$, which is decomposition product of LiPF$_6$. [14, 15, 19, 46], and hydrolysed LiPF$_6$, Li$_x$PF$_y$O$_z$. [13, 15]

Similar to the 500 cycle cathode, two sets of doublet peaks with similar binding energy are observed on the 500 cycled anode. It is interesting to note that the phosphate was already present on the as-

received anode, which may have formed during the formation process. The phosphate component in the 500 cycle anode is 6 times higher (1.8 at %) than the as-received anode (0.3 at %).

The increase of phosphates in both the cathode and anode after cycling is consistent with literature findings [13, 14, 19, 46]. Leroy et al investigated the formation of SEI using XPS and atomic force microscopy (AFM) at different potentials (3.0-4.2 V) of the first and fifth cycles on the graphite electrode and showed the decomposition of $LiPF_6$ mainly occurred when charged to 4.2 V. [19]

Co $2p$ spectra corresponding to $LiCoO_2$ (LCO) for as-received and aged cathode show complex multiplet peaks splitting, Fig. 6 (c). Two broad asymmetric peaks were observed at 779.7 eV and 794.8 eV which correspond to Co $2p_{3/2}$ and Co $2p_{1/2}$, respectively, Fig. 6 (c). Shake-up satellite peaks from the Co $2p_{3/2}$ energy level were also observed, indicative Co in a positively charged oxidation state. The intensity of the peaks for the 500 cycle cathode is lower than the as-received cathode due to attenuation from thicker CEI layer, which obscure the LCO active material surface and reduce its detection signal. The spectra for Co $2p_{3/2}$ is fitted parameters developed by Biesinger et al [47] which take into account the asymmetry of the main envelope, surface and bulk plasmon loss and the shake-up satellite peaks. Co $2p_{3/2}$ spectra for both the as-received and 500 cycled cathodes fit well with Co_3O_4 model, with Co^{2+}/Co^{3+} mixed oxidation state. Note Co $2p$ spectra in this study are very similar to those reported in the literature but there is no mention of Co^{2+} before the sample is aged [13-15, 37]. Takamatsu et al [18] reported a 3 nm thick oxide layer such as Co_3O_4 due to Co reduction on the LCO cathode surface when immersed in 1M $LiClO_4$ 1:1 volume ratio of ethylene carbonate and diethyl carbonate electrolyte. Therefore it is likely that the Co $2p$ signal is from this oxide layer rather than LCO bulk surface. Nevertheless, further investigation is required to verify this. In addition, it is worth noting no Co is detected in both as-received and aged anode, which indicates no Co dissolution, due to overcharging, has occurred during cell cycling.

3.5 Scanning Electron Microscopy (SEM)

Fig. 7 (a), (b) and (c) shows the scanning electron microscope images of the cathode, anode and separator of the as-received Fitbit cell and the same cell components after 500 charge-discharge cycles. Fig. 7 (a) reveals no significant topographical difference between the cathode materials of the as-received and 500 cycled samples. Both samples have large grain size variation ranging from 1 to 15 μm. EDS reveals the cathode materials to be lithium cobalt oxide (LCO), not shown. Closer inspection on the 500 cycles sample shows possible degradation product on the cathode surface, however, the size is beyond the detectable limit of EDS.

Fig. 7 (b) shows the microstructure of the as-received and 500 cycled anodes. Both samples show a similar grain size ranging from 10 to 20 μm. Many small crystalline particles were observed on the surface of the 500 cycled sample which were not seen on the as-received sample. The higher magnification image shows these particles are angular in shape and with particles size in the 0.1-0.5 μm range. EDS mapping, shown in Fig. 7 (e) reveals these particles to be fluorine rich and, as indicated by XPS analysis, Fig. 6 (a), they are very likely to be LiF. This is in contrast to the as-received sample, Fig. 7 (d) which shows a more even fluorine distribution throughout the whole sample, most likely due to the present of PVdF binder - $(C_2H_2F_2)_n$- , which is also observed in XPS analysis. Detailed EDS mapping can be found in supplementary material Fig. S2 and Fig. S3. LiF particles are not observed in the as-received anode which could simply due to only small amount of LiF being present (2 at % as detected by XPS).

Fig. 7 (c) shows the SEM images of the separator from the as-received and 500-cycled sample, with no significant visible difference after cycling. The non-symmetrical porous structure of the separator suggest that it is made by a wet process [5, 48]. EDS mapping, Fig. S4, shows that silicon is well dispersed on the separator and the separator may have been grafted with siloxane by electron beam irradiation [49]. It has been reported that the grafted PE separator with siloxane has a higher operating voltage (5.2 V) before the onset of electrolyte oxidation in LCO/graphite cell, as opposed to non-

grafted PE separator which is stable up to 4.5 V and thus has better retention capacity [49]. Nevertheless, further investigation is required to work out the composition of the separator.
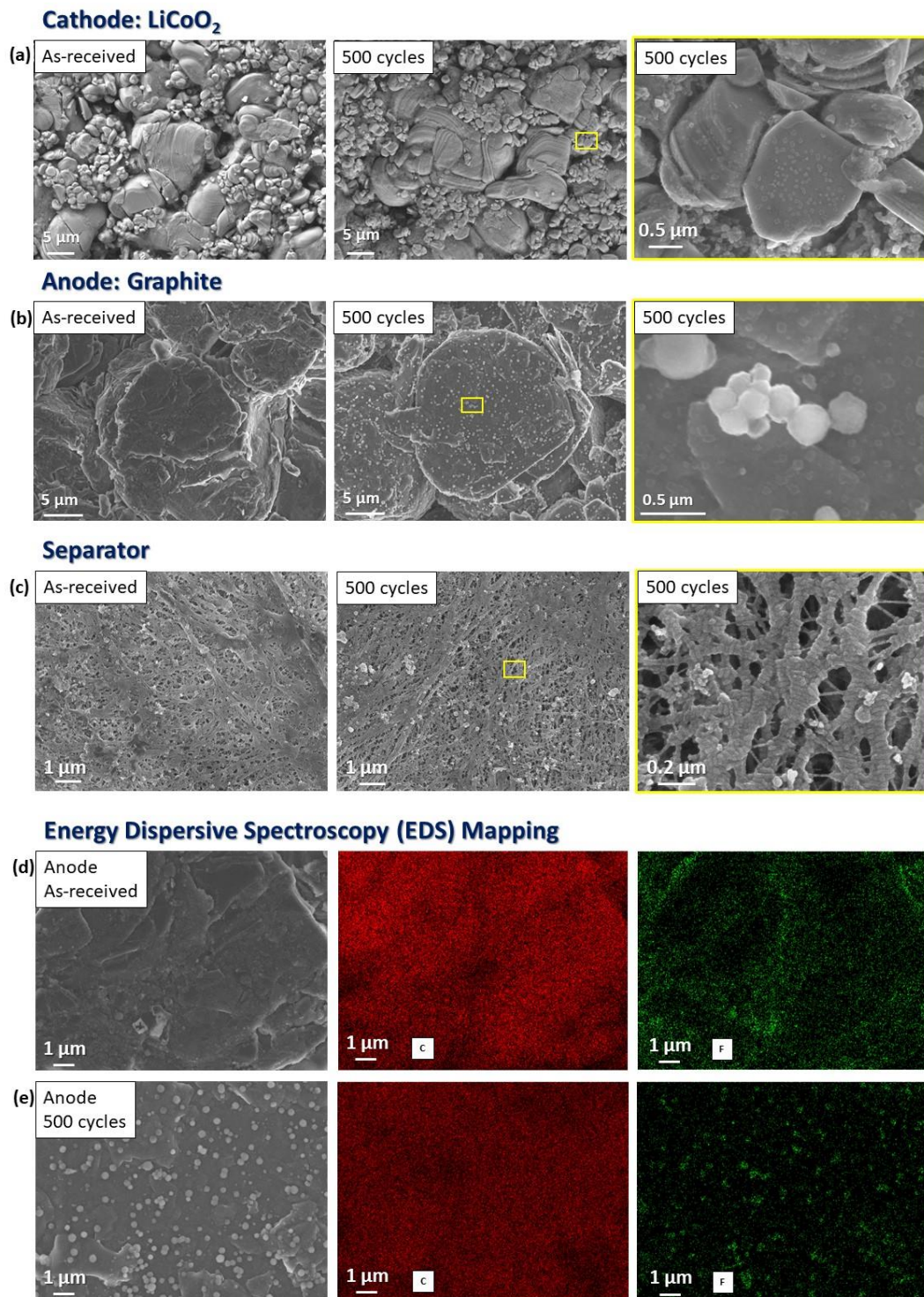

Fig. 7 *Scanning electron microscope (SEM) images of (a) cathode (b) anode and (c) separator of as-received and 500 cycled Fitbit cells. Energy dispersive spectroscopy (EDS) mapping for (d) as-received and (e) 500 cycled Fitbit anode.*

3.6 Li$^+$ Charge Transfer Resistance (R$_{ct}$)

Nyquist plots for the Fitbit cell at different cycle numbers at 3.5 V and 4.3 V are shown in Fig. 8 (a) and 8 (b), interpreted using the EIS model [50] shown in Fig. 8 (c). Both EIS spectra show two overlapping semicircles with a non-zero intercept at the real impedance axis (Z') and comparison of R$_{ohm}$, R$_{SEI}$, and R$_{ct}$ extracted from the EIS circuit model. The non-zero intercept at the real axis (Z') corresponds to the ohmic resistance (R$_{ohm}$), in which the resistance corresponds to combination of electrolyte, connectors and the current collector. The semicircle at the higher frequency range corresponds to resistance of the solid electrolyte interface (R$_{SEI}$) whereas the lower frequency semicircle corresponds to the Li-ion charge transfer (R$_{ct}$) between the electrode and the electrolyte interface. Overall, the cell impedance at 3.5 V is higher than at 4.3 V, and the total cell impedance increases with increasing cycle number. Impedance spectra were fitted using the equivalent circuit model shown in Fig. 8(d) and the resistance measurements for each component at 3.5 V and 4.3 V are shown in Fig. 8 (a) and 8 (b), respectively. All three components show an increase in resistance, but R$_{ct}$ increased by 195 % and 149 % at 3.5 V and 4.3 V, respectively after 500 cycles.

The increase in R$_{ohm}$ indicates degradation of the electrolyte and coating delamination while the increase in R$_{SEI}$ indicates the possibilities of surface layer (anode and cathode) growth or the presence of a more insulating phase in the surface layer. However, the large increase in R$_{ct}$ indicates that the main degradation is due to a side reaction occurring at the electrode/electrolyte interface resulting in a by-product which is inhibiting the Li$^+$ ion charge transfer process. This finding is consistent with the reported literature. [6-12].

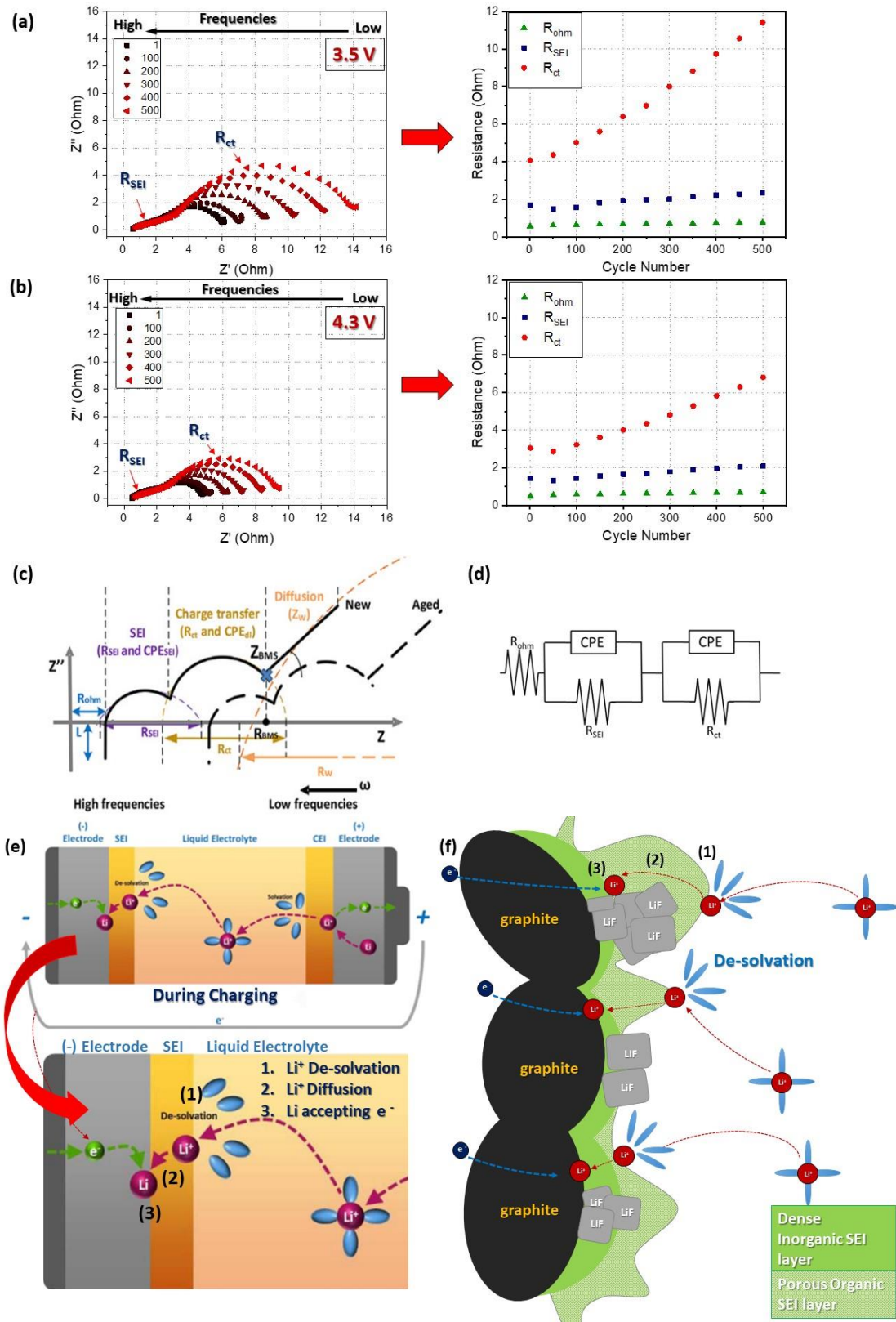**Fig. 8** *Nyquist plots and R_{ohm}, R_{SEI}, and R_{ct} extracted from EIS circuit model for Fitbit cell at (a) 3.5 V and (b) 4.3 V at different cycle number. (c) Typical EIS spectrum of a lithium ion cell [50]. (d) EIS equivalent circuit model used for analysis. (e) Schematic view of Li+ charge transfer process [23] and (f) SEI involving charge transfer process on graphite particles.*

XPS shows the inner CEI/SEI layer composed more of solvent reduction product, but the outer surface layer has an increasing amount of $LiPF_6$ decomposition product such as LiF and phosphates. LiF is evident by SEM on the Fitbit anode surface. Previous work suggests that the presence of LiF on graphite [51] and on the $LiCoO_2$ surface [10, 13-16, 19, 37] in $LiPF_6$ based electrolyte systems inhibits the diffusion of Li^+ ions through the electrode-electrolyte interface, thus resulting in capacity loss [7, 17, 25]. Strmcnik et al [52] recently reported experiment data showing the formation of LiF by an electrocatalytic process through transformation of HF to LiF and H_2. Detailed reactions are shown as below:

$$LiPF_6 \rightarrow LiF + PF_5 \hspace{4cm} \text{(Equation 1)}$$

$$H_2O + PF_5 \rightarrow 2HF + POF_3 \hspace{3cm} \text{(Equation 2)}$$

$$HF + e^- \rightarrow H_{ad} + F^- \hspace{4cm} \text{(Equation 3)}$$

$$2H_{ad} \rightarrow H_2 \hspace{5.5cm} \text{(Equation 4)}$$

$$F^- + Li^+ \rightarrow LiF_{(s)} \hspace{4.5cm} \text{(Equation 5)}$$

where H_{ad} is the adsorbed reactive intermediate. The amount of LiF is dictated by the HF inventory in the cell and LiF [52] starting to form at 0.25 V in graphene/Li and HOPG (highly orientated pyrolytic graphite)/Li [52] and 3.8-4.2 V in LCO/graphite full cell [19]. It is therefore very likely the LiF formation in Fitbit Cell is related to the dissociation of the HF when charging at higher voltage (4.35 V) allowing F^- to react with Li^+ at the electrode/electrolyte interface to form LiF as proposed by Strmcnik et al [52]. DFT calculations by Pan and Cheng show the much lower ionic conductivity of LiF on the cathode (10^{-31} Scm^{-1}) than on the anode (10^{-12} Scm^{-1}) [26], which implies that even a thin LiF layer on the cathode can affect a huge impact on the charge transfer resistance, which not even a thick LiF layer on the anode can achieve. LiF has an electron tunnelling barrier of 3.98 eV (6.26 HSE) and 2 nm thick of LiF is sufficient to block electron tunnelling [53], which could lead to further parasitic reactions [22]. Admittedly this model is based on a dense, continuous LiF film on the electrode surface. Unfortunately, detection of continuous nanometer thick LiF is beyond the limit of SEM, nevertheless granular crystals

LiF are observed on the anode. Strmcnik et al. [52] also reported porous and granular (grain size 10-30 nm) LiF on their graphene and HOPG anodes as opposed to a smooth compact LiF film on Ir (111), Au (111), Pt (111) and Cu (111) substrates. Because of its porous nature, it is believed that the LiF film may still be permeable by electrolyte and that LiF will not further passivate reactions of HF with Li$^+$ or solvent reduction at the graphite/electrolyte interface [52] and such an inhomogeneous distribution would result in variable electron tunnelling possibilities. Growth of surface layers on electrodes is well-accepted as being one of the common ageing processes in lithium ion batteries [22, 31, 54]. XPS indicates that active materials become obscured, embedded by the growth of the surface layer and this increases the SEI resistance, as shown in EIS measurements.

Therefore, one of the ageing mechanisms for Fitbit cell due to continual growth of CEI and SEI layer and theincreasing amount of insulating LiF granular crystals on the outer layers inhibits Li$^+$ flux, diffusion through thicker surface layers and thus increases the degree of charge transfer resistance, Fig. 8 (e) and (f).

As mentioned in the introduction, cobalt oxide formation on the cathode surface and internal strain accumulation within cathode grains due to phase transition can also contribute to charge transfer resistance. Structural transformations in LCO have been reported elsewhere [55] and are generally attributable to:

(i) Surface film formation as a result of oxidation at the electrode-electrolyte interface.

(ii) Structural or phase changes in the active material from a hexagonal to a cubic (spinel) structure.

Both of these effects will result in increases in the charge transfer resistance, as evident in Figure 8, and will be more pronounced at higher temperatures. Temperature measurements were not carried out during this study but it would be useful to establish what temperatures are reached inside these cells as it could be a significant ageing factor.

To effectively verify surface phase changes requires techniques such as x-ray absorption near edge structure, to determine the oxidation state of Co on the surface and in the bulk LCO, and utilising

transmission electron microscopy (TEM) to establish any possible spinel formation on the surface of the LCO grains and thus further investigation is required.

4. Conclusions

Ageing analysis on Fitbit cells that had undergone charge/discharge cycling at variable C-rate and fixed rate cycling for 500 cycles, were performed utilising XCT, EIS, SEM with EDS and XPS. Fitbit cells showed 82 % capacity retention after 500 cycles with average coulombic efficiency of 99.89 %. However, the unravelling of the cell contents shows severe anode coating delamination from the Cu current collector due to the high bending stress exerted on the cell components when rolled to a 3 mm diameter jelly roll. This may be due to the defective coatings remaining sufficiently compressed and in electrical contact to form a seemingly still intact jelly roll with minimised adverse effects from physical damage. That there is a side-specific degradation dominance (in terms of electrode coating damage) requires further investigation to confirm our proposals here and such explorations are compelling from a future electrode design perspective.

The increase in charge transfer resistance is related to the increase of surface film layer thicknesses of the SEI and CEI, which increase the distance for Li^+ ion diffusion. Insulating LiF crystals on the outer surface layer of the electrode inhibits or reduced the surface area for Li^+ ion transportation.

Co $2p$ spectra shows good fitting to the Co_3O_4 model and prompts further investigation using XANES and TEM to verify this finding, examine the bulk material and also to understand the impact of the formation of transition metal oxide surface on the LCO surface on the cell performance.

This study could also open up exciting areas in battery manufacturing to address winding issues for cylindrical cells (especially miniaturised formats). For example, highlighting the need to understand whether there is merit in varying the coating properties on each side of double-sided coating for wound cylindrical cells, in order to improve the mechanical resilience of coatings that have asymmetric stresses exerted on them.

Declaration of competing interest

The authors declare that they have no known competing financial interests or personal relationships that could have appeared to influence the work reported in this paper.

CRediT authorship contribution statement

C.C. Tan: Investigation, Formal analysis, Writing - original draft. **M. Walker:** Investigation, Formal analysis, Writing - review & editing. **G. Remy:** Investigation, Formal analysis, Writing - original draft. **N. Kourra:** Investigation, Formal analysis. **F. Maddar:** Writing - review & editing. **S. Dixon:** Investigation. **M. Williams:** Resources. **M.J. Loveridge:** Conceptualization, Supervision, Funding acquisition, Writing - review & editing.

5. References

[1] Y. Wang, B. Liu, Q. Li, S. Cartmell, S. Ferrara, Z.D. Deng, J. Xiao, Journal of Power Sources, 286 (2015) 330-345.
[2] J. Song, X. Yang, S.-S. Zeng, M.-Z. Cai, L.-T. Zhang, Q.-F. Dong, M.-S. Zheng, S.-T. Wu, Q.-H. Wu, Journal of Micromechanics and Microengineering, 19 (2009) 045004.
[3] P.A. Nelson, K.G. Gallagher, I.D. Bloom, D.W. Dees, Modelling the Performance and Cost of Lithium-ion Batteries for Electric-drive Vehicles, Second edition, Argonne National Laboratory, 2012 ANL-12/55.
[4] S. Tintignac, R. Baddour-Hadjean, J.-P. Pereira-Ramos, R. Salot, Electrochimica Acta, 60 (2012) 121-129.
[5] L. Wang, B. Chen, J. Ma, G. Cui, L. Chen, Chemical Society Reviews, 47 (2018) 6505-6602.
[6] D. Zhang, B.S. Haran, A. Durairajan, R.E. White, Y. Podrazhansky, B.N. Popov, Journal of Power Sources, 91 (2000) 122-129.
[7] B. Markovsky, A. Rodkin, Y.S. Cohen, O. Palchik, E. Levi, D. Aurbach, H.J. Kim, M. Schmidt, Journal of Power Sources, 119-121 (2003) 504-510.
[8] E.E. Levin, S.Y. Vassiliev, V.A. Nikitina, Electrochimica Acta, 228 (2017) 114-124.
[9] X. Wang, X. Zheng, Y. Liao, Q. Huang, L. Xing, M. Xu, W. Li, Journal of Power Sources, 338 (2017) 108-116.
[10] J.-N. Zhang, Q. Li, Y. Wang, J. Zheng, X. Yu, H. Li, Energy Storage Materials, 14 (2018) 1-7.
[11] S.Y. Vassiliev, V.V. Sentyurin, E.E. Levin, V.A. Nikitina, Electrochimica Acta, 302 (2019) 316-326.

[12] K.J. Nelson, J.E. Harlow, J.R. Dahn, Journal of The Electrochemical Society, 165 (2018) A456-A462.

[13] R.A. Quinlan, Y.-C. Lu, D. Kwabi, Y. Shao-Horn, A.N. Mansour, Journal of The Electrochemical Society, 163 (2016) A300-A308.

[14] Y.-C. Lu, A.N. Mansour, N. Yabuuchi, Y. Shao-Horn, Chemistry of Materials, 21 (2009) 4408-4424.

[15] S. Verdier, L. El Ouatani, R. Dedryvère, F. Bonhomme, P. Biensan, D. Gonbeau, Journal of The Electrochemical Society, 154 (2007) A1088-A1099.

[16] K. Edström, T. Gustafsson, J.O. Thomas, Electrochimica Acta, 50 (2004) 397-403.

[17] D. Aurbach, B. Markovsky, A. Rodkin, E. Levi, Y.S. Cohen, H.J. Kim, M. Schmidt, Electrochimica Acta, 47 (2002) 4291-4306.

[18] D. Takamatsu, Y. Koyama, Y. Orikasa, S. Mori, T. Nakatsutsumi, T. Hirano, H. Tanida, H. Arai, Y. Uchimoto, Z. Ogumi, Angewandte Chemie International Edition, 51 (2012) 11597-11601.

[19] S. Leroy, F. Blanchard, R. Dedryvère, H. Martinez, B. Carré, D. Lemordant, D. Gonbeau, Surface and Interface Analysis, 37 (2005) 773-781.

[20] R. Dedryvère, S. Laruelle, S. Grugeon, L. Gireaud, J.-M. Tarascon, D. Gonbeau, Journal of The Electrochemical Society, 152 (2005) A689-A696.

[21] E. Peled, S. Menkin, Journal of The Electrochemical Society, 164 (2017) A1703-A1719.

[22] E. Peled, Journal of The Electrochemical Society, 126 (1979) 2047-2051.

[23] T.R. Jow, S.A. Delp, J.L. Allen, J.-P. Jones, M.C. Smart, Journal of The Electrochemical Society, 165 (2018) A361-A367.

[24] M. Gauthier, T.J. Carney, A. Grimaud, L. Giordano, N. Pour, H.-H. Chang, D.P. Fenning, S.F. Lux, O. Paschos, C. Bauer, F. Maglia, S. Lupart, P. Lamp, Y. Shao-Horn, The Journal of Physical Chemistry Letters, 6 (2015) 4653-4672.

[25] J.L. Tebbe, A.M. Holder, C.B. Musgrave, ACS Applied Materials & Interfaces, 7 (2015) 24265-24278.

[26] J. Pan, Y.-T. Cheng, Y. Qi, Physical Review B, 91 (2015) 134116.

[27] D. Aurbach, B. Markovsky, G. Salitra, E. Markevich, Y. Talyossef, M. Koltypin, L. Nazar, B. Ellis, D. Kovacheva, Journal of Power Sources, 165 (2007) 491-499.

[28] E. Markevich, G. Salitra, D. Aurbach, Electrochemistry Communications, 7 (2005) 1298-1304.

[29] A. Yano, M. Shikano, A. Ueda, H. Sakaebe, Z. Ogumi, Journal of The Electrochemical Society, 164 (2017) A6116-A6122.

[30] R. Yazami, Y. Ozawa, H. Gabrisch, B. Fultz, Electrochimica Acta, 50 (2004) 385-390.

[31] J.-H. Shim, J.-M. Han, J.-H. Lee, S. Lee, ACS Applied Materials & Interfaces, 8 (2016) 12205-12210.

[32] H. Wang, Y.I. Jang, B. Huang, D.R. Sadoway, Y.M. Chiang, Journal of The Electrochemical Society, 146 (1999) 473-480.

[33] M. Zou, M. Yoshio, S. Gopukumar, J.-i. Yamaki, Chemistry of Materials, 15 (2003) 4699-4702.

[34] Z. Chen, J.R. Dahn, Electrochimica Acta, 49 (2004) 1079-1090.

[35] Z. Chen, J.R. Dahn, Electrochemical and Solid-State Letters, 7 (2004) A11-A14.

[36] Y. Jin, N. Li, C.H. Chen, S.Q. Wei, Electrochemical and Solid-State Letters, 9 (2006) A273-A276.

[37] A.T. Appapillai, A.N. Mansour, J. Cho, Y. Shao-Horn, Chemistry of Materials, 19 (2007) 5748-5757.

[38] T. Guan, S. Sun, F. Yu, Y. Gao, P. Fan, P. Zuo, C. Du, G. Yin, Electrochimica Acta, 279 (2018) 204-212.

[39] J. Chen, J. Liu, Y. Qi, T. Sun, X. Li, Journal of The Electrochemical Society, 160 (2013) A1502-A1509.

[40] J. Hu, Y. Wang, D. Li, Y.-T. Cheng, Journal of Power Sources, 397 (2018) 223-230.

[41] S.-J. Lee, in: 2016 AIMCAL Web Coating and Handling Conference 2016.

[42] L. Yang, Z.-C. Zhong, Y.-C. Zhou, W. Zhu, Z.-B. Zhang, C.-Y. Cai, C.-S. Lu, Acta Mechanica Sinica, 32 (2016) 342-348.

[43] J.N. Reimers, J.R. Dahn, Journal of The Electrochemical Society, 139 (1992) 2091-2097.

[44] D. Mohanty, E. Hockaday, J. Li, D.K. Hensley, C. Daniel, D.L. Wood, Journal of Power Sources, 312 (2016) 70-79.

[45] L. David, R.E. Ruther, D. Mohanty, H.M. Meyer, Y. Sheng, S. Kalnaus, C. Daniel, D.L. Wood, Applied Energy, 231 (2018) 446-455.

[46] A.M. Andersson, D.P. Abraham, R. Haasch, S. MacLaren, J. Liu, K. Amine, Journal of The Electrochemical Society, 149 (2002) A1358-A1369.

[47] M.C. Biesinger, B.P. Payne, A.P. Grosvenor, L.W.M. Lau, A.R. Gerson, R.S.C. Smart, Applied Surface Science, 257 (2011) 2717-2730.

[48] H. Lee, M. Yanilmaz, O. Toprakci, K. Fu, X. Zhang, Energy & Environmental Science, 7 (2014) 3857-3886.

[49] J.Y. Lee, Y.M. Lee, B. Bhattacharya, Y.-C. Nho, J.-K. Park, Electrochimica Acta, 54 (2009) 4312-4315.

[50] C. Pastor-Fernández, K. Uddin, G.H. Chouchelamane, W.D. Widanage, J. Marco, Journal of Power Sources, 360 (2017) 301-318.

[51] A.M. Andersson, K. Edström, Journal of The Electrochemical Society, 148 (2001) A1100-A1109.

[52] D. Strmcnik, I.E. Castelli, J.G. Connell, D. Haering, M. Zorko, P. Martins, P.P. Lopes, B. Genorio, T. Østergaard, H.A. Gasteiger, F. Maglia, B.K. Antonopoulos, V.R. Stamenkovic, J. Rossmeisl, N.M. Markovic, Nature Catalysis, 1 (2018) 255-262.

[53] A. Wang, S. Kadam, H. Li, S. Shi, Y. Qi, npj Computational Materials, 4 (2018) 15.

[54] P. Verma, P. Maire, P. Novák, Electrochimica Acta, 55 (2010) 6332-6341.

[55] F. Leng, C.M. Tan, M. Pecht, Scientific Reports, 5 (2015) 12967.